



Supplementary Materials for

Enhanced water permeability and tunable ion selectivity in subnanometer carbon nanotube porins

Ramya H. Tunuguntla,* Robert Y. Henley,* Yun-Chiao Yao,
Tuan Anh Pham, Meni Wanunu, Aleksandr Noy[†]

*These authors contributed equally to this work.

[†]Corresponding author. Email: noy1@llnl.gov

Published 25 August 2017, *Science* **357**, 792 (2017)

DOI: 10.1126/aan2438

This PDF file includes:

Materials and Methods
Supplementary Text
Figs. S1 to S17
Table S1
References

Materials and Methods

Carbon nanotube porin (CNTP) synthesis

1,2-dioleoyl-sn-glycero-3-phosphocholine lipid (DOPC) used in this study was obtained from Avanti Polar Lipids. 1.5 nm diameter carbon nanotubes (CNTs) were obtained from Nano-Lab Inc. (Cat. No. D1.5L1-5-S) and 0.8 nm diameter CNTs were obtained from Sigma-Aldrich, Inc. (Cat. No. 773735). The carbon nanotube porins were prepared and purified by methods detailed by Tunuguntla et al (35). In brief, 28 or 36 mg of DOPC lipid, for 0.8 nm or 1.5 nm CNTP synthesis, respectively, was added to a 20 mL glass scintillation vial from DOPC lipid stock solution (25 mg/mL DOPC, in chloroform) and the solvent was evaporated using a rotary evaporator (RotaVap, BUCHI) for 10 min. Trace solvent in the vial was further evaporated in a vacuum desiccator overnight. Then, 0.7 (for 0.8 nm CNTs) or 1 mg (for 1.5 nm CNTs) was baked on a hotplate in ambient air at 474.3 °C and 461.5 °C, respectively, for 60 mins to remove non-graphitic impurities. 14 mL of Milli-Q water was added to the purified CNTs, and that mixture was added to the corresponding dried lipid film. The CNT/lipid complex was bath-sonicated for 20 min (Emerson Electric Co., Model Branson 1510) to disperse the CNTs in the lipid solution. This was followed by probe-sonication using a ¼ inch sonicator micro-tip (QSonica) at 203 W power for 16 hrs at 3-second pulses with a 1-second pause between each pulse. To purify the shortened CNTPs, the sonication-processed solution was transferred to 15mL conical centrifuge tubes and centrifuged at 10,300×g for 1hr at 20 °C followed by a 28,000×g spin for 10 min at 20 °C. After centrifugation, the supernatant containing the CNTP was carefully aspirated with a glass pipette and stored at 4 °C. This sonochemical method of cutting regularly produces a mean of 10.6 ± 2.3 nm length CNTPs as confirmed by cryo-TEM imaging and Raman spectroscopy analysis performed in previous studies (36, 37).

Determining CNTP synthesis yield and CNTP density in liposomes

For each batch of CNTPs that were produced for experimental use, we analyzed the product immediately after sonication processing using a CNTP proton permeability assay (36), as a benchmark of the CNTP activity and to quantify the average number of porins incorporated into a 200 nm liposome, incorporation efficiency (I.E.).

Briefly, to determine the I.E. of a given porin batch, we made LUVs and CNT-LUVs encapsulating a pH-sensitive pyranine dye (8-Hydroxypyrene-1,3,6-trisulfonic acid, trisodium salt) containing buffer made as 10 mM pyranine, 10 mM HEPES, 150 mM NaCl, 30 mM KCl at pH 7.51. Subsequently, we carried out an acid titration with 1 µL of 1 M HCl into a known volume of solution containing LUVs. This titration led to a stepwise reduction in the intravesicular pH, and the resulting step changes in pyranine fluorescence are recorded. The fluorescence data were converted to luminal pH readings over the pH range of 6.9-7.51, where the pyranine fluorescence emission was linearly proportional to the solution pH. For a typical batch activity measurement, 2 mL of buffer (10 mM HEPES, 150 mM NaCl, 30 mM KCl) at pH 6.9 was added to a cuvette and placed in a Fluoromax-4 fluorimeter (Jobin-Yvon) at room temperature for at least 5 minutes with constant stirring until a steady baseline measurement is reached. We then quickly added 70 µL (pH 7.51) of the CNTP-LUVs to the cuvette and monitored the changes in fluorescence intensity of entrapped pyranine (ex. 450 nm, em. 514 nm) to determine the kinetics of the pH gradient dissipation through the CNTP pore. All

measurements took place in dark conditions with constant stirring. We then extracted the slope of each curve (dpH/dt) from the transport assay in the pH range of 7.51–6.9, and then converted the measured proton permeability into the number of CNTPs per vesicle using the unitary proton permeabilities of CNTPs determined (36) in our previous work, 1.80×10^{-7} and 3.30×10^{-7} nS per 1.5 nm (wCNTP) and 0.8 nm (nCNTP) diameter CNTP, respectively.

CNTP reconstitution into liposomes

The DOPC lipid in chloroform was aliquoted (2 mg) into glass vials and the solvent was evaporated under a stream of argon gas or air and then further dried overnight in a vacuum desiccator chamber. Liposomes were prepared by adding 1 mL of 10 mM HEPES, pH 7.8 buffer to the dried lipid film to obtain a final lipid concentration of 2 mg/mL. To incorporate CNTPs into the liposomes, we first dried 2 mL of the appropriate CNTP solution overnight in a vacuum desiccator to remove the solvent. The dried CNTP film was hydrated with 1 mL of 10 mM HEPES, pH 7.8 buffer and bath-sonicated for 30 seconds to ensure the film is completely solubilized and detached from the glass vial. This solution was subsequently used to hydrate a 2mg DOPC lipid film and bath-sonicated to mix thoroughly. The liposome solutions were hydrated at room temperature for 30 minutes. To ensure formation of large unilamellar vesicles (LUVs) or CNTP-LUVs, the samples underwent 10 cycles of freeze-thaw treatment where the liposomes were flash-frozen in liquid nitrogen and subsequently thawed at 50°C. The LUVs or CNTP-LUVs were then extruded 21 times through a 200 nm pore-sized polycarbonate membrane using a mini-extruder (Avanti Polar Lipids). To separate free, unincorporated CNTPs from the liposome solution, we performed size exclusion chromatography (SEC) with a column containing Sepharose CL-6B (Sigma-Aldrich, St. Louis, MO) agarose, and collected fractions in a 96-well plate while using 10 mM HEPES pH 7.8 buffer as an eluent. Fractions containing liposomes were pooled. In the case of measurements performed at pH 3, the preparation of CNT-LUVs or LUVs was carried out as previously described (at pH 7.8) followed by diluting the sample 10-fold into 10 mM HEPES buffer at pH 2.5 and incubating it for 3 hours to allow the pH inside and outside the liposomes to equilibrate. The final pH was verified with a pH probe. We determined the CNTP activity and liposome incorporation efficiency with a proton permeability assay that we developed and described previously (36).

Dynamic light scattering (DLS) and zeta potential measurements

Average liposome diameters were determined by DLS with a Malvern Instruments Zetasizer Nano-ZS90. Typically, 70 μ L of the liposome sample was added to a disposable small volume cuvette (BRAND GmbH & Co. KG, Germany) and light scattering intensity of the liposomes was measured. Each size reading was obtained from an average of 10 individual measurements. The Zetasizer instrument was also used to measure the zeta potential as an indirect measure of surface charge density. For those measurements, 1 mL of a sample was loaded into a disposable folded capillary zeta cell, and zeta potential measurements were recorded from an average of 100 readings per sample.

CNT porin water permeability measurements

Water permeabilities of 1.5 or 0.8 nm CNTPs or pure liposomes were measured using a stopped-flow instrument (SFM2000, BioLogic). The liposome samples were rapidly mixed with a hypertonic solution that caused them to shrink due to the osmotic gradient driving a water efflux. The hyperosmolar buffer contained 10 mM HEPES, with the pyranine osmolyte concentration ranging from 5.95 - 95 mM at pH 7.8. The osmolarity of each buffer was verified with a freezing-point osmometer (Osmomat 3000, Gonotec). A typical experiment for a permeability assay consists of mixing the liposomes (0.5 mg/mL DOPC) with osmolyte buffer at a ratio of 1:7 (38 μ L: 266 μ L) and a flow rate of 8 mL/s. Note that we take into account the dilution factor of the osmolyte buffer when calculating the final osmotic strength of the solution. Under these experimental conditions, a reduction in liposome volume led to an increase in the light scattering signal, according to the Rayleigh-Gans-Debye (RGD) theory of light scattering (38). We recorded light scattering data at 594 nm, a 90° scattering angle, with an acquisition interval between 50-200 μ s, and a measured dead time of 0.7 msec. For each osmolyte concentration, we averaged at least 5-8 individual runs. For experiments including kosmotropic and chaotropic additives, the osmolyte buffer contained 150 mM concentration of tetraethylene glycol (PEG₄), glucose, urea, or trehalose.

Osmotic water permeability of LUVs or CNTP-LUVs, P_f , in units of cm/s was calculated using the following expression:

$$P_f = \frac{k}{\left\{ \left(\frac{SA}{V_0} \right) (V_w) (C_{out} - C_{in}) \right\}} \quad [1]$$

where $k = -(\Delta V/V_0)/t$ is the shrinkage rate determined by single or double exponential fits to the light scattering data for LUVs or CNTP-LUVs, respectively, SA/V_0 is the ratio of liposome surface area to initial volume, V_w is the partial molar volume of water (18 cm³), and $(C_{out} - C_{in})$ is the difference in osmolarity between the intravesicular and extravesicular aqueous solution. Here we assume that change in intensity of the scattered light is proportional to the change in the vesicle volume ($\Delta V/V_0$), which validates the Boyle-van't Hoff law (39). A similar assumption has been used in and verified by several previous studies (40-44). For liposomes containing CNTPs, the stopped flow scattering curves could be fit to a double exponential function with two kinetic rates – a smaller k_1 , that represented water efflux through the phospholipid bilayer of the liposome, and a larger k_2 , that represented water efflux through the porins (k_2 is also the parameter that increased with increasing CNTP density. For each CNTP-LUV, the single-channel unit water permeability, P_w , for either 1.5 or 0.8 nm CNTPs, was calculated as the difference in permeability, p_f , between CNTP-LUVs and LUVs under the same osmotic gradient, multiplied by the surface area of the CNT-LUV (SA), and divided by the number of porins incorporated in the liposome for a given batch of CNTPs, I.E.:

$$P_w = (p_f^{CNTP-LUV} - p_f^{LUV}) * \frac{SA_{CNTP}}{I.E.} \quad [2]$$

Aquaporin-1 (AQP1) water permeability

Aquaporin-1 protein used in this study was obtained from MyBiosource, Inc. (Cat. No: MBS948542) at a concentration of 5 mg/mL. DOPC proteoliposomes containing aquaporin-1 protein were prepared using the detergent-mediated reconstitution method

(45) at a protein: lipid molar ratio of 1:3,052 using the following procedure: 80 μ L DOPC lipid solution (25 mg/mL) in chloroform was dried to a lipid film on a glass vial using a steady stream of argon, hydrated with 1 mL of 10 mM HEPES-K, 0.05% dodecyl- β -D-maltopyranoside (β -DDM) buffer pH 7.8 to a final concentration of 2 mg/mL lipid, and bath-sonicated for 10 mins, extruded 20 times through 200-nm polycarbonate membranes (Avanti Polar Lipids). Next, 5 μ L of AQP1 stock solution was added to the lipid-detergent mixture and incubated at room temperature for 45 mins. To ensure complete removal of the detergent to form proteoliposomes, we used polystyrene Biobeads SM2 (Bio-Rad, Hercules, CA), which were thoroughly washed using the Holloway method (46), which consisted of washing with 100% methanol two times, deionized water three to four times, and then equilibrating in 10 mM HEPES-K buffer. Biobeads (160 mg/mL) were added to the lipid-AQP1-detergent mixture and gently stirred at room temperature for 6 h, during which time the solution was transferred into a fresh batch of Biobeads each hour, followed by the final incubation with a fresh batch of Biobeads overnight at 4°C under gentle stirring. Successful incorporation of AQP1 into liposomes was verified using UV-Vis spectroscopy. The sample was passed through an SEC column, eluted with 10 mM HEPES-K buffer at pH 7.8, and fractions containing liposomes were pooled. The proteoliposomes were diluted 3-fold prior to performing water permeability measurements using the stopped-flow apparatus. The final AQP1 channel density (ca. 117 AQP1 monomers/liposome) was calculated from the vesicle diameter (as measured by DLS), AQP1 concentration, lipid concentration, and area per lipid molecule (47).

Activation energy measurements

To determine activation energies for water transport we repeated water permeability measurements for LUVs and CNTP-LUVs at different temperatures in the interval between 10 and 50 °C. For these experiments the solution reservoirs and the measurement cell of the stopped-flow instrument was maintained at a set temperature by a recirculating heater/chiller (Polystat, Cole Parmer). Permeability rates through CNTPs (after subtracting the background liposome permeability), measured at varying temperatures, were then used to construct an Arrhenius plot. Activation energy was also measured for AQP1 in a similar manner to validate our experimental procedures.

Nanopore chip fabrication

A 500 μ m-thick and 100 mm diameter silicon <100> wafer was cleaned with a standard RCA process, rinsed with deionized water, and spun dry prior to LPCVD. Then, the wafer was immediately placed in a LPCVD furnace (MRL industries) and 50 nm of SiN_x was deposited on either side of the wafer, followed by the thermally deposited 2 μ m-thick SiO₂ film on both sides. The positive e-beam resist ZEP520-A was spun on to one side of the wafer and baked for 2 min at 170 °C. Then, an electron-beam lithography (EBL) pattern, comprising an array of ca. 200 nm-diameter circles and two alignment marks were exposed in JEOL 6300FS e-beam writer. The alignment marks were used to line up with photolithography marks later in the fabrication process to ensure that each EBL circle would be aligned with a SiN_x membrane. Next, the exposed EBL pattern was developed in ZED-N50 for 1 min and dried under gentle stream of nitrogen followed by rinsing with isopropanol. Prior to photolithography on the other side of the wafer, the

developed pattern was inspected in high-resolution optical microscopy to verify the proper exposure and development. Afterwards, the SiN_x was etched with SF₆ plasma in Technics Micro-RIE series 800 to fabricate ~200 nm-diameter through-holes on the EBL-processed side of the wafer. Photolithography was used on the other side of the wafer to define the pattern for KOH etching down to membrane using custom made photomask. First, Shipley Microposit S1818 positive photoresist was spun on the other side (non EBL side) of the wafer and baked for 1 min at 115 °C. Next, the pattern was exposed in Suss MicroTech MA/BA 6 contact aligner using a photomask with alignment marks. These alignment marks are identical to those written during EBL exposure. Following successful backside alignment and exposure, the pattern was developed in MicroDev for 1 min. Then, the SiN_x was etched with SF₆ plasma in Technics Micro-RIE Series 800 for KOH etching down to freestanding SiN_x membrane through exposed windows. Then the photoresist was stripped off using acetone and the wafer was mounted in Idonus PEEK backside protection wafer holder such that photolithography side is exposed. The wafer in one-sided holder was placed in 40% KOH at 65 °C overnight to etch the exposed silicon squares down to SiO₂ layer followed by removing 2.5 μm-thick SiO₂ film using buffered oxide etch. Once all silicon was completely etched away in KOH, then the other 2.5 μm-thick SiO₂ layer was removed using BOE. The wafer was soaked in ZDMAC (Zeon, Co., Japan) and N-methyl pyrrolidone (NMP) for several hours at 50 °C to strip off the e-beam resist. This process results in a wafer of ~200 chips, each with SiN_x freestanding membrane containing ~200 nm-diameter through-hole. Prior to use, individual nanopore chips were cleaned and rendered hydrophilic by immersion in a heated piranha solution (1:2 H₂O₂:H₂SO₄) for 10 minutes. Chips were then thoroughly rinsed in heated DI water and stored in DI water.

Conductance and reversal potential measurements

Nanopore chips were dried under a vacuum and mounted in a PTFE cell using a quick-curing silicone gasket (Smooth-On EcoFlex 5) to seal the chip and reduce the capacitance (48). The two chambers of the PTFE cell were then filled with an electrolyte solution and Ag/AgCl electrodes are placed in each chamber. The current passing through the nanopore was measured using an Axon Axopatch 200B amplifier (Molecular Devices) and digitized using an Axon Digidata 1550b (Molecular Devices) at a sampling rate of 100 kHz and low-pass filtered between 1-10 kHz as noted in the text. Transmembrane current was measured in 10 mV increments between -200 mV and 200 mV, this data was then used to fit to a conductance model based on pore geometry to approximate the pore diameter (typically ~200 nm).

Liposomes made from DOPC: cholesterol 90:10 (mole %) were fused to the chip to create solvent-free bilayers that spanned and sealed the SiN nanopores. Prior to liposome addition both chambers of the cell were filled with 100 mM KCl, 10mM Tris, and 1mM EDTA at pH 7.5. Liposomes were then added to the *cis*-chamber, where they experience osmotic stress as a result of their contents being hyperosmotic to the surrounding solution, causing them to burst over the chip surface to create a supported bilayer that spans the nanopore (49, 50). Sufficient sealing of the nanopore was confirmed with conductance measurements (with the typical bilayer conductance of ~6 pS). Zwitterionic DOPC lipids are used to ensure that the charge on the bilayer does not affect the selectivity of the CNTPs (51).

CNTPs were incorporated into a liposome bilayer as described in the previous section, and fused onto the chip surface. Alternatively, CNTPs were directly added to the *cis*- chamber of the cell after lipid bilayer formation, where they spontaneously inserted into the membrane. After incubation, both chambers were thoroughly flushed with buffer a minimum of 4 times using a syringe pump (kdScientific, LEGATO110). I-V curve measurements were then taken in 10 mV increments. The current was allowed to equilibrate for 2 seconds after each change in applied voltage to minimize errors due to the capacitance of the substrate. The conductance was estimated from the I-V curves using a linear least square regression.

For reversal potential measurements the chambers were filled with different salt solutions as noted in the text. To prevent the generation of a redox potential at the electrodes during these measurements, we connected electrode to the chamber using agarose salt bridges (5% agarose, 1M KCl). In these cases, both electrodes were immersed in a solution of 1M KCl, 10mM Tris, and 1mM EDTA at pH 7.5. In instances when salt bridges were not used, the I-V curves were corrected for the redox potential of the electrodes by shifting the I-V curve by the theoretical value for the redox potential, both methods produced results in good agreement with one another (Fig. S12). Theoretical redox potential values were calculated using the Nernst equation (Eq. 3).

$$\Delta E = \frac{RT}{F} \ln \frac{a_{cis}}{a_{trans}} \quad [3]$$

where ΔE is the theoretical potential offset observed at the electrodes, R is the gas constant, T is the temperature of the solution, F is the Faraday constant, and a is the activity of the ionic species (52). The reversal potential was then used with the Goldman-Hodgkins-Katz equation (Eq. 4) to extract the transference numbers for the membrane (53).

$$V_R = (2t_{+M} - 1) \frac{RT}{F} \ln \frac{a_{cis}}{a_{trans}} \quad [4]$$

where V_R is the measured reversal potential, and t_{+M} is the effective transference number for the membrane. With knowledge of the effective cation transference number for the membrane, and the cation transference number in the bulk solution, the permselectivity of the membrane was calculated using Eq. 5.

$$P = \frac{t_{+M} - t_{+S}}{1 - t_{+S}} \quad [5]$$

where, P is the permselectivity, and t_{+S} is the cation transference number in the bulk solution. The ionic selectivity ratio, SR (cation/anion), was calculated using Eq. 6.

$$SR = \frac{t_{+M}}{1 - t_{+M}} \quad [6]$$

Computational Methods

The confined solutions in the wide and narrow CNTs were represented by tetragonal supercells constructed from a unit of (6,5) and (19,0) CNT primitive cells with diameters of 0.8 nm and 1.4 nm, respectively. Dimensions of the supercell that represents the

narrow CNT are $a=b=18.52 \text{ \AA}$, $c=40.679 \text{ \AA}$, while the corresponding values for the wide CNT are $a=b=21.17 \text{ \AA}$, $c=17.06 \text{ \AA}$. The supercells contained 13 and 56 water molecules, respectively, yielding the density of bulk water at ambient conditions (1.0 g/cm^3).

The first-principles simulations were carried out using Born-Oppenheimer molecular dynamics with the Qbox code (<http://qboxcode.org/>), in which the electronic ground state wave functions were optimized at every ionic step. The Brillouin zone was sampled at the Γ point. The interatomic force was derived from density functional theory (DFT) and the Perdew, Burke and Ernzerhof (PBE) approximation for the exchange-correlation energy functional (54). The interaction between valence electrons and ionic cores was represented by norm-conserving pseudopotentials Ry. All hydrogen atoms were replaced with deuterium to maximize the allowable time step, which was chosen to be 10 a.u.

We equilibrated the solutions at a constant temperature of 400 K for 10 ps. An elevated temperature was chosen as the employment of the PBE approximation is known to yield an over-structured liquid water at ambient conditions, and the use of a simulation temperature around 400 K was shown to recover the experimental liquid structure at $T=300 \text{ K}$ (21, 55). Statistics were collected over 25 ps. To validate the first principles model, we verified that it reproduces the value of the bulk water diffusion coefficient (55).

Supplementary Text

Vesicle water permeability dependence on osmotic gradient value

Stopped-flow based water transport measurements in LUVs (in presence and in absence of CNTPs in the lipid shell) under different osmotic gradients show decreasing bulk permeability values (Fig 1A,B, also Fig S1). For example, for control LUVs the permeability value, p_f , varies from 1.3×10^{-2} to $0.7 \times 10^{-2} \text{ cm/s}$ with increasing gradient size (from 5.95 to 95 mM). Vesicles are not infinitely compressible and there is a structural resistance barrier that prevents vesicle shrinkage beyond a certain point, producing an apparent decrease in water permeability with an increasing osmolyte concentration (56). To obtain the *true* bulk water permeability, p_w , that is independent of applied osmotic stress, we fit our data to a model, described by Verkman *et al.* (57), which describes structural resistance as a second barrier in series with the vesicle membrane:

$$P_f = \left(\frac{1}{p_{LUV}} + R(C_0 - C_i) \right)^{-1} \quad [7]$$

Using this model, we obtained water permeability of $1.4 \times 10^{-2} \text{ cm/s}$ for DOPC liposomes, which agrees well with previously reported values (58, 59). To account for the added permeability of the CNTPs in the lipid shell we modified the model to include an additional term, p_{CNTP} :

$$P_f = \left(\frac{1}{(p_{LUV} + p_{CNTP})} + R(C_0 - C_i) \right)^{-1} \quad [8]$$

Equations 7 and 8 allowed us to extract values of p_{CNTP} , and p_{LUV} from the experimental data (Figure S2 A, B). The bulk permeability data for CNTP-LUVs containing 1.5 or 0.8 nm CNTPs, along with the measured CNTP density per vesicle and vesicle size, were used to calculate (eq. 2) the single CNTP (unit) water permeabilities, P_{CNTP} , for each CNTP size.

Comparison of measured single channel water permeabilities with Poiseuille's law prediction

Hydrodynamic laws of laminar water flow can be applied to the water flow through nanotube channels or membrane proteins, under the condition that the pores are large enough to contain multiple molecules of water that bear properties similar to those of bulk water. Poiseuille's law can be used to calculate single-channel permeability coefficients by correlating the number of water molecules that pass through a pore per second to the pore length and radius (60). Under the assumptions that the pore is static and cylindrical, the single-channel permeability coefficient, P_w , for a pore radius, r , and length, l , is given by: $P_w = (\pi R T r^4 / \eta l V_w)$. Although this equation was developed for macroscopic pore sizes where the finite radius of a water molecule, r_w , is neglected, it has been modified to include correction factors (61, 62) that account for: (a) steric restrictions of water molecules entering the pore and (b) increased frictional interactions between water and pore walls. This modified equation for water permeability is as follows:

$$P_w = \frac{\pi R T r^4}{8 \eta l V_w} \left[2 \left(1 - \frac{r_w}{r} \right)^2 - \left(1 - \frac{r_w}{r} \right)^4 \right] \left[1 - 2.104 \left(\frac{r_w}{r} \right) + 2.09 \left(\frac{r_w}{r} \right)^3 - 0.95 \left(\frac{r_w}{r} \right)^5 \right] \quad [9]$$

For 1.5 nm diameter CNTP Eq. 9 predicts a single-channel permeability coefficient of $3.8 \times 10^{-13} \text{ cm}^3/\text{s}$, which agrees closely our measured value of $2.19 \pm 0.05 \times 10^{-13} \text{ cm}^3/\text{s}$, as well as with the permeability the values from previous reports of graphene and protein channels of similar sizes (60, 63, 64). These comparisons support our conclusion that the physical properties of water inside these porins are similar to that of bulk water. We stress that this formalism does not apply to 0.8 nm diameter CNTPs where water structure is significantly different from that of bulk water.

Water Diffusion Coefficients in CNTPs

We can calculate the diffusion coefficient, D_w , for water transport from unitary permeability rates of the CNTPs. For 1.5 nm diameter wCNTPs, the continuum theory should be still applicable (60) and we can use the following equation to calculate diffusion coefficient for water:

$$D_{w,1.5} = \frac{l}{A_c} (P_f) \quad [10]$$

where l is the channel length, and A_c is cross-sectional area of the channel.

For 0.8 nm nCNTPs, the continuous approximation is no longer valid as we cannot assume that the water density in the pore is the same as in bulk and must take into

account the fixed distance between the single-file water molecules and the volume they occupy. The mobility of single-file water molecules, $D_{w,0.8}$, is better described by the Einstein relation (19, 33, 65):

$$D_{w,0.8} = \frac{z^2 P_w}{2v_w} \quad [11]$$

where z and v_w are the average distance between two water molecules in the single-file water wire, and the molecular volume of one water molecule ($v_w = V_w/N_A$), respectively.

Water structure in CNTPs

Computed oxygen-oxygen radial distribution functions ($g_{oo}(r)$) of water molecules (Fig. S16) reveal more details of the water structure in CNTs. As expected, water structure in nCNTs deviates significantly from the bulk; showing that the first solvation shell is not recovered with a slightly larger position of the $g_{oo}(r)$ first maximum. In contrast, the $g_{oo}(r)$ for water in wCNTs is much closer to the bulk result, showing that water in those wider CNT channels retains almost bulk-like structure.

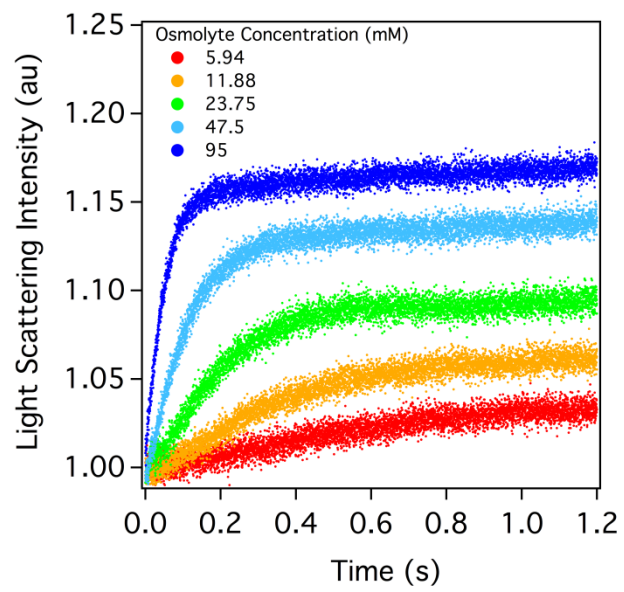


Fig. S1.

Light scattering traces collected after exposing DOPC liposomes to increasing levels of osmotic pressure. Legend indicates concentrations of pyranine osmolyte.

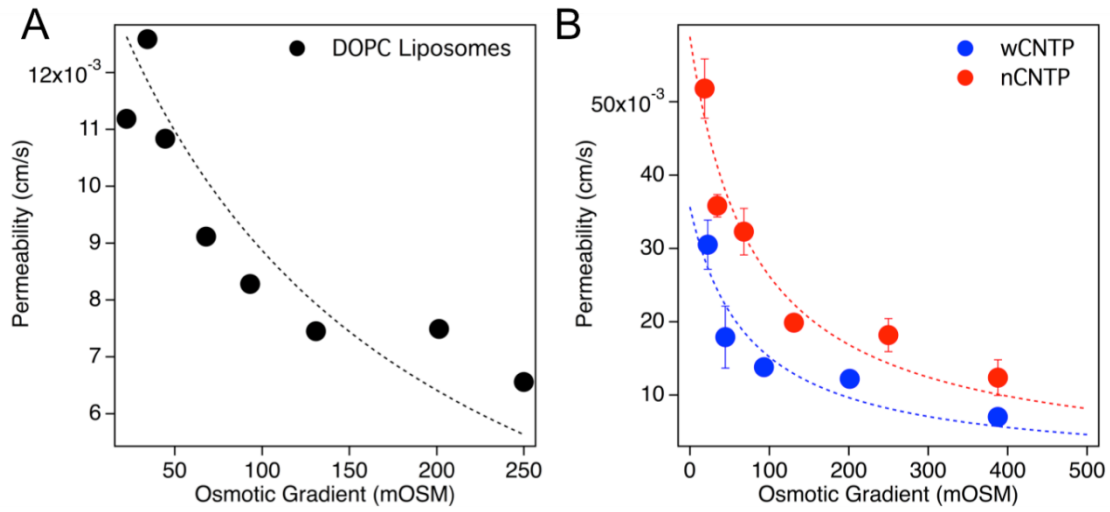


Fig. S2.

Water permeability of **(A)** DOPC liposomes and **(B)** DOPC liposomes containing CNTPs measured in stopped-flow experiments as a function of applied osmotic pressure.

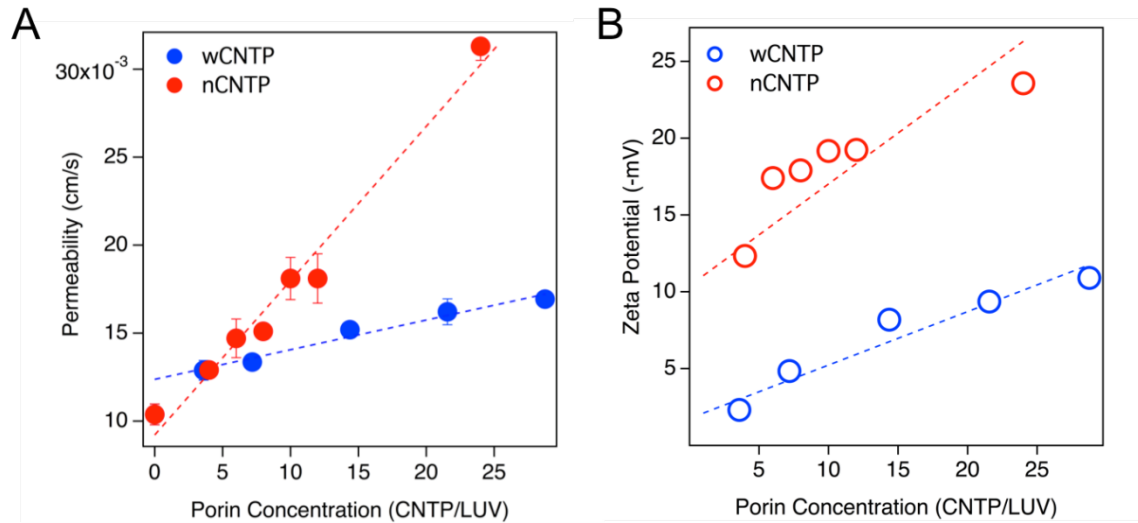


Fig. S3.

(A) Water permeability of CNTP-containing liposomes plotted as a function of CNTP concentration. Higher CNTP loading leads to increased overall liposome permeability. (B) Zeta-potential of CNTP-containing liposomes (pH 7.8) plotted as a function of the CNTP concentration. Increased loading with negatively-charged CNTPs increases the negative zeta-potential of the liposomes.

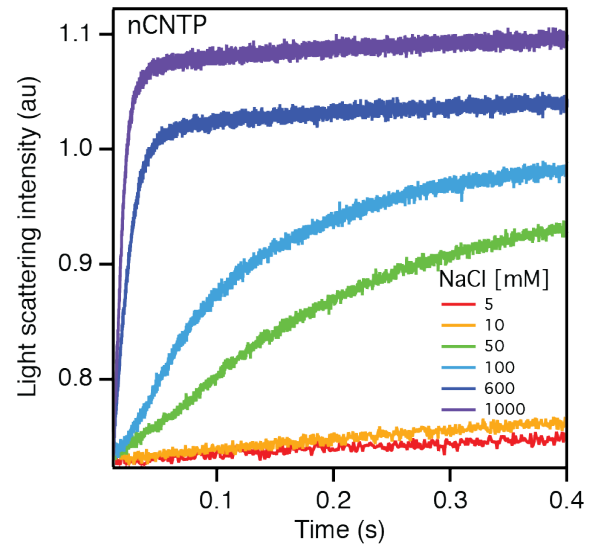


Fig. S4.

Light scattering traces showing water permeability through 0.8 nm CNTPs when osmotic pressure is generated from NaCl osmolyte (5-1000 mM).

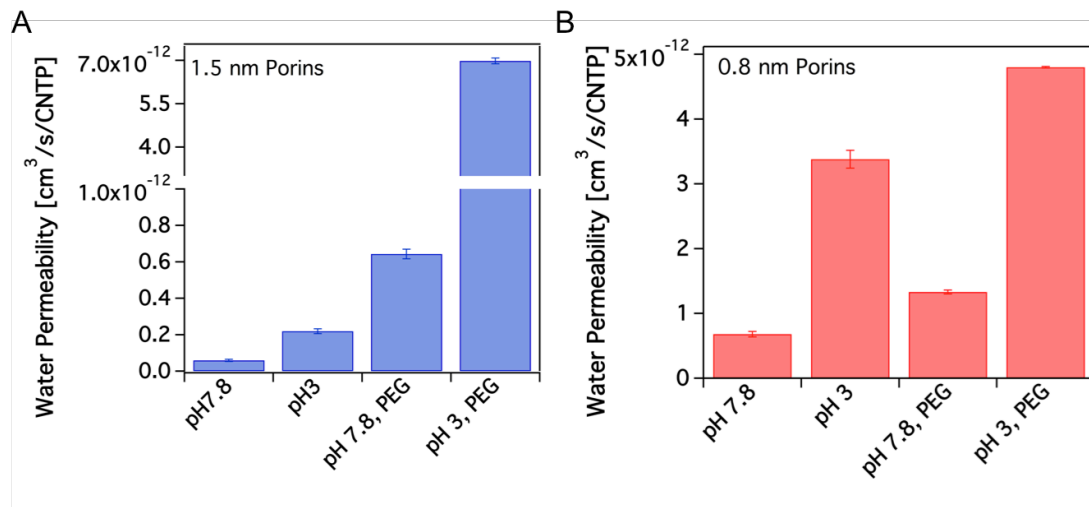


Fig. S5.

Water permeability through (A) wCNTP and (B) nCNTPs measured at pH 3 and pH 7.8 with and without addition of 150 mM PEG chaotrope (N=3).

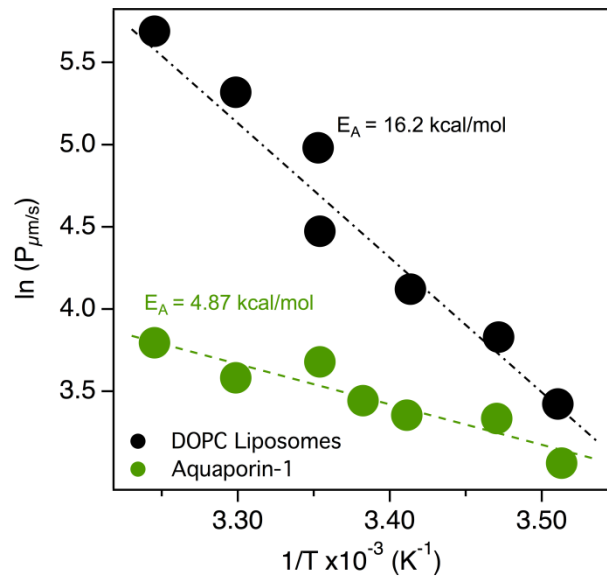


Fig. S6.

Arrhenius plot showing the temperature dependence of the water permeability of DOPC liposomes and aquaporin-1 channels. Measurements were performed at pH 7.8 and the activation energies, determined from the slope of linear regression of the data, are consistent with previously reported values (34, 44) for DOPC liposomes (16.2 kcal/mol, black circles) and AQP1 channels (4.87 kcal/mol, green circles).

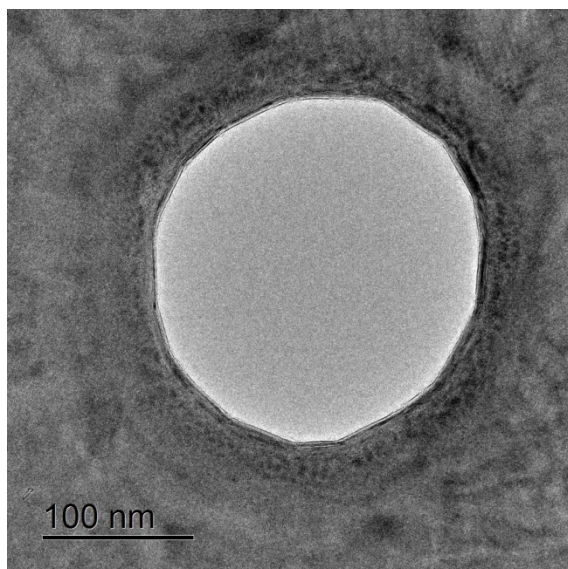


Fig. S7.

TEM image of ca. 200 nm diameter nanopore fabricated in SiN_x membrane.

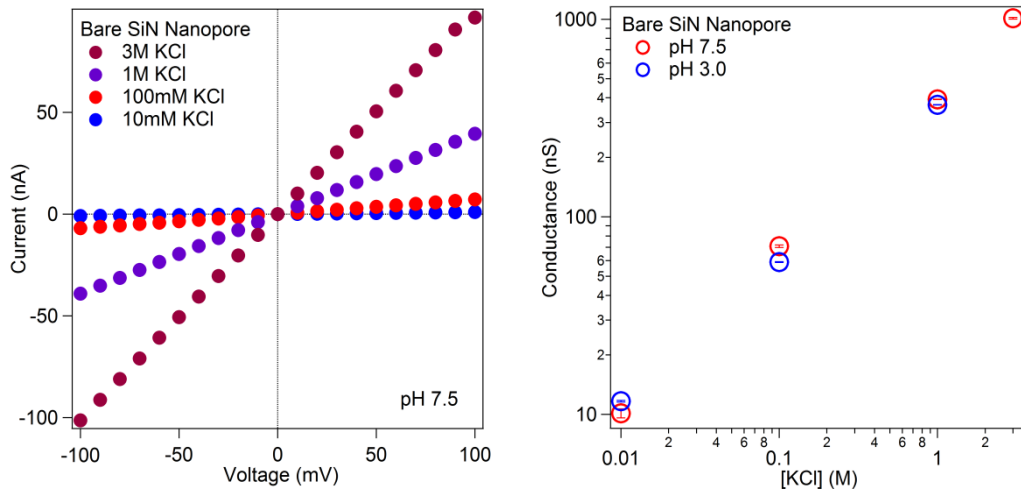


Fig. S8.

I-V curve measurements for the bare SiN 200 nm nanopore (left). The device displays the expected linear relationship between conductance and KCl electrolyte concentration (right).

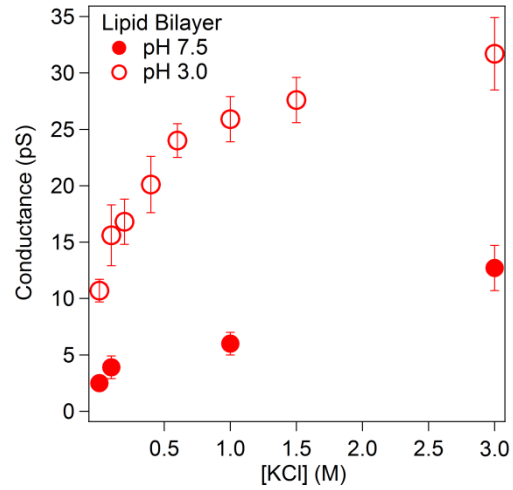


Fig. S9.

Plot of conductance values measured at different KCl concentration for a nanopore sealed with a lipid bilayer. Conductance was determined as the slope of I-V curves. Measured conductance values are significantly lower than those of CNTP-containing bilayers and do not display the same scaling with salt concentration.

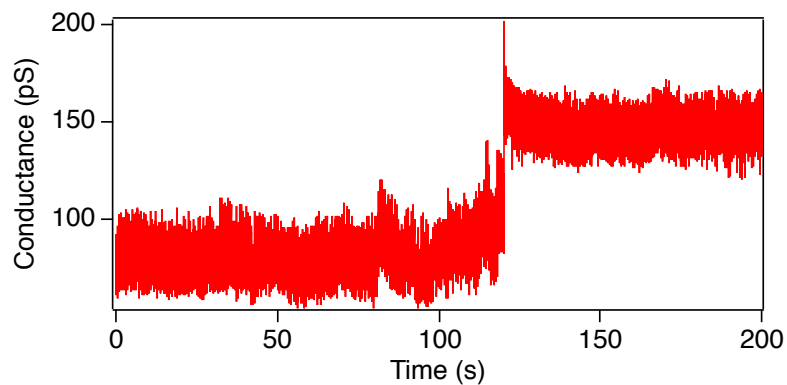


Fig. S10.

Example trace showing the insertion of a single nCNTP into the solvent-free lipid bilayer formed via the vesicle fusion method. Data was taken in a buffer containing 1 M KCl, 10 mM Tris, and 1 mM EDTA at pH 7.5 with an applied voltage of 100 mV. The trace shows a stepwise conductance increase of ca. 65 pS. In this trace, one nCNTP was already present in the bilayer before the start of current recording.

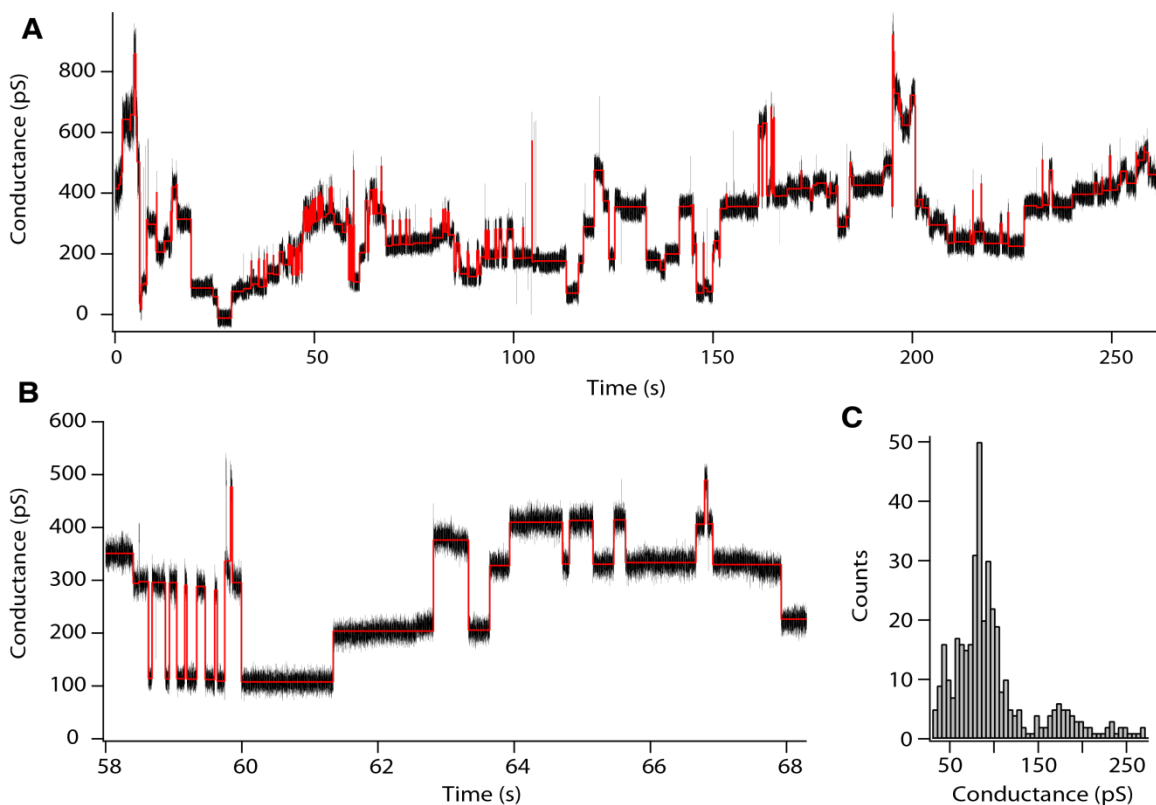


Fig. S11.

(A,B) Example traces and (C) a histogram of conductance jump values from nCNTP insertions in lipid bilayers formed by the painting method. The bilayer was formed as detailed in previous study (35). Bilayers are formed using the Montal-Mueller technique, as described by Gutsman et al (66). Data was taken in a buffer containing 1 M NaCl, 10 mM Tris, and 1 mM EDTA at pH 7.5 with an applied voltage of 100 mV. Conductance jumps are of similar value to those observed in solvent free bilayers made with the liposome fusion method described earlier (Fig. 3C), but were much less stable. Stability may be hindered by interactions between the residual solvent in the bilayer and the lipid-wrapped CNTPs. Traces were analyzed using a custom Python CUSUM software to extract stepwise conductance increases.

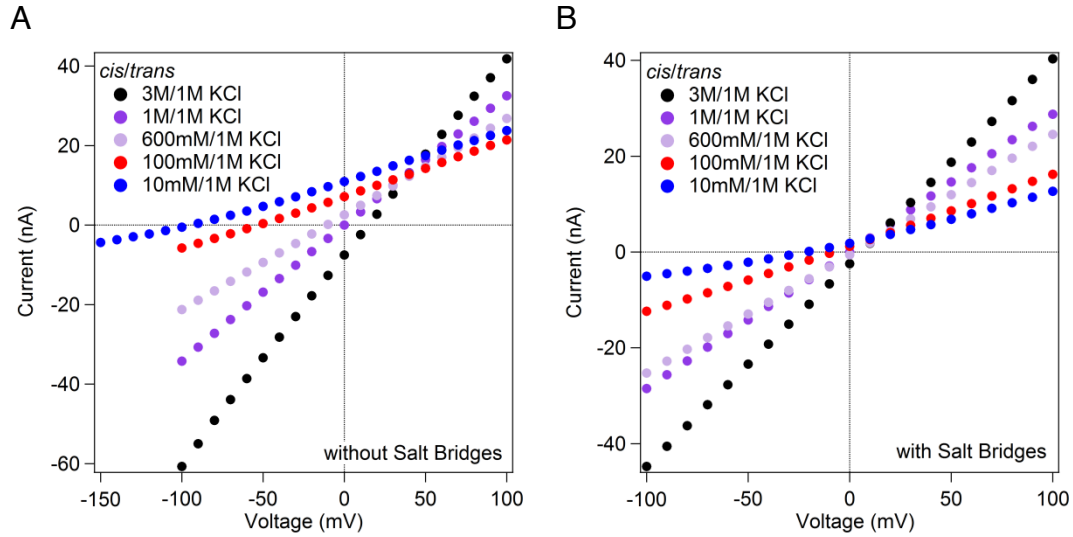


Fig. S12.

Reversal potential measurements for a bare SiN_x 200 nm diameter nanopore at pH 7.5 where electrodes were either **(A)** directly immersed into the chambers, or **(B)** connected to them via salt bridges. Both measurements are in good agreement after correction for the theoretical Nernst potential. The legend indicates KCl electrolyte concentration in the *cis*- and *trans*- compartments of the measurement cell. The bare nanopore substrate shows very weak anion selectivity (Cl⁻/K⁺ selectivity ratios of 2.12, 4.54, 5.88, for *cis* concentrations of 10 mM, 100 mM, and 3 M respectively).

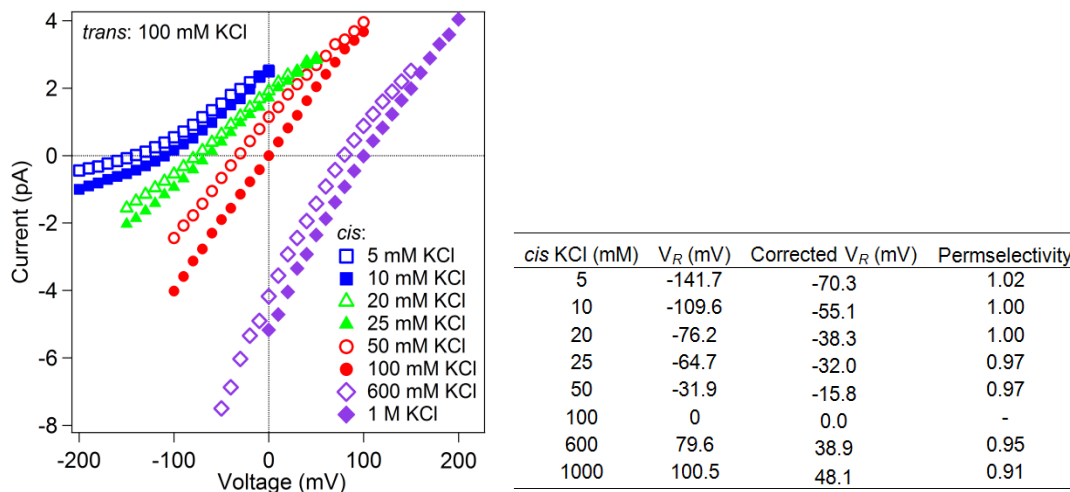


Fig. S13.

I-V curve measurements (left) for nCNTPs obtained when the electrodes were connected directly to the measurement chamber compartments (i.e. without the use of salt bridges). From the reversal potentials, V_R , permselectivity values were calculated after correcting for the theoretical Nernst potential, as indicated in the table (right).

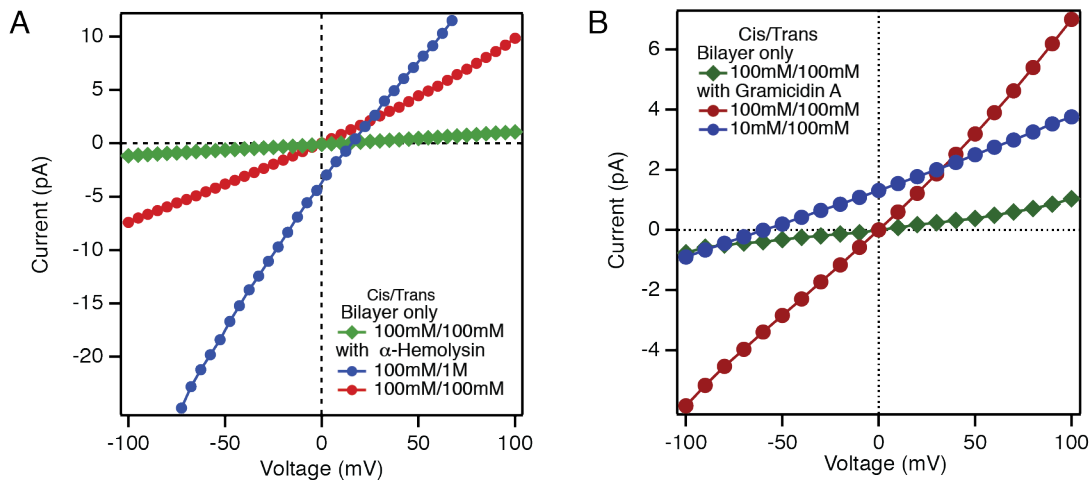


Fig. S14.

(A) I-V curve measurement (red circles) and reversal potential measurement (blue circles, obtained without using salt bridges) on a lipid bilayer with inserted α -hemolysin channels, and an I-V curve recorded on a pure lipid bilayer prior to protein insertion (green diamonds). Reversal potential value of 15.6 mV corresponds to a K^+/Cl^- selectivity ratio of 0.54, in good agreement with the results reported by the Bayley group (67). (B) An I-V curve measurement (red circles) and reversal potential measurement (blue circles, performed with salt bridges) on a lipid bilayer with inserted gramicidin channels, and an I-V curve recorded on a pure lipid bilayer prior to gramicidin insertion (green diamonds). Measured reversal potential value of -57.47 mV indicates complete rejection of anions (K^+/Cl^- ratio of ∞), in good agreement with literature reports for gramicidin (68). For all measurements, the ion gradient values are indicated in the figure legend. In addition to specified concentrations of KCl all solutions contained 10 mM Tris, 1 mM EDTA, pH 7.5.

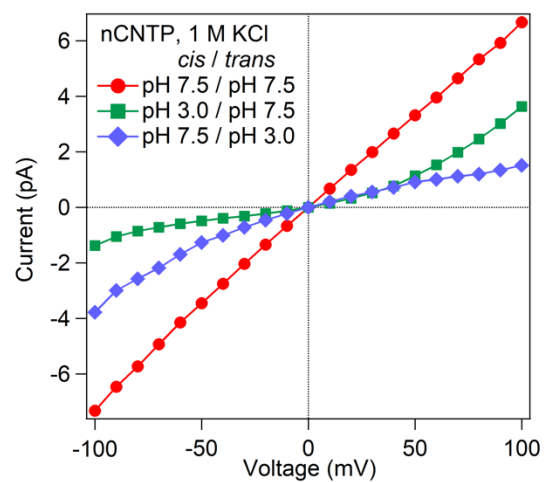


Fig. S15.

I-V curves recorded when different sides of nCNTP were exposed to 1 M KCl concentration under symmetric and asymmetric pH conditions (as indicated in the figure legend).

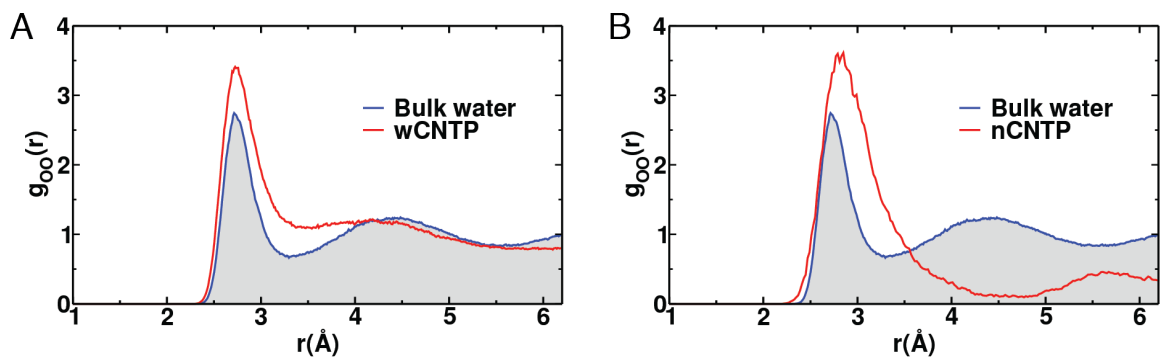


Fig. S16.

Calculated oxygen-oxygen radial distribution function $g_{oo}(r)$ for water molecules in the bulk and in (A) wCNT and (B) nCNT.

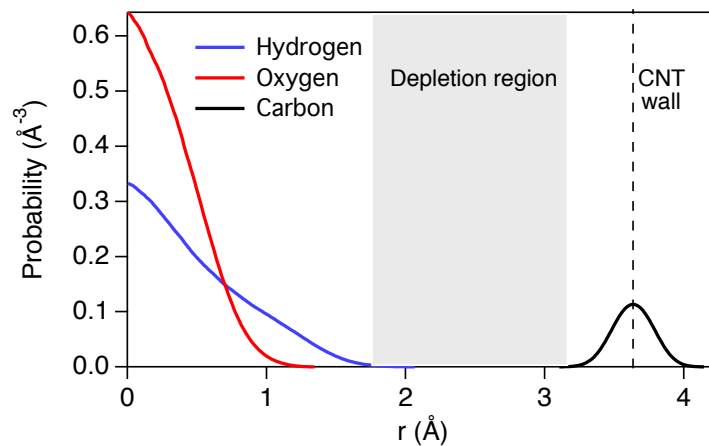


Fig. S17.

Radial atomic density distribution functions of oxygen (red), hydrogen (blue), and carbon (black) in a 0.8 nm CNT, as obtained with first-principles simulations. The carbon wall is indicated by the dashed line, and the origin is the center of the CNT. The gray shaded area indicates the depletion layer between water molecules and CNT wall.

Table S1.

Reversal potential, permselectivity, and selectivity ratio values for different values of salt gradient across the bilayer membrane with incorporated nCNTPs.

High Salt/ Low salt (mM)	pH 7.5			pH 3		
	Reversal Potential (mV)	Permselectivity	Selectivity Ratio (K ⁺ /Cl ⁻)	Reversal Potential (mV)	Permselectivity	Selectivity Ratio (Cl ⁻ /K ⁺)
3000/1000	-21.9	0.832	10.6	10.1	-0.354	2.2
3000/10	-108.0	0.813	9.5	-	-	-
1000/600	-11.2	0.956	44	-	-	-
1000/100	-49.8	0.952	40	32.6	-0.591	4.3
1000/50	-67.5	0.986	140	-	-	-
1000/25	-87.2	1.028	∞	-	-	-
1000/20	-91.8	1.017	∞	-	-	-
1000/10	-106.5	0.996	522	75.1	-0.669	5.7
1000/5	-124.2	1.003	∞	-	-	-
600/100	-40.3	0.989	184	17.6	-0.404	2.5
100/50	-16.6	1.028	∞	-	-	-
100/25	-34.2	1.060	∞	-	-	-
100/20	-38.6	1.020	∞	-	-	-
100/10	-56.8	1.040	∞	47.6	-0.836	15
100/5	-70.6	0.989	162	-	-	-
50/10	-38.0	0.988	159	-	-	-
20/10	-17.0	1.020	∞	-	-	-

References

1. M. M. Mekonnen, A. Y. Hoekstra, Four billion people facing severe water scarcity. *Sci. Adv.* **2**, e1500323 (2016). doi:10.1126/sciadv.1500323 [Medline](#)
2. C. J. Vörösmarty, P. Green, J. Salisbury, R. B. Lammers, Global water resources: Vulnerability from climate change and population growth. *Science* **289**, 284–288 (2000). doi:10.1126/science.289.5477.284 [Medline](#)
3. Y. X. Shen, P. O. Saboe, I. T. Sines, M. Erbakan, M. Kumar, Biomimetic membranes: A review. *J. Membr. Sci.* **454**, 359–381 (2014). doi:10.1016/j.memsci.2013.12.019
4. P. Agre, L. S. King, M. Yasui, W. B. Guggino, O. P. Ottersen, Y. Fujiyoshi, A. Engel, S. Nielsen, Aquaporin water channels—From atomic structure to clinical medicine. *J. Physiol.* **542**, 3–16 (2002). doi:10.1113/jphysiol.2002.020818 [Medline](#)
5. C. Y. Tang, Y. Zhao, R. Wang, C. Helix-Nielsen, A. G. Fane, Desalination by biomimetic aquaporin membranes: Review of status and prospects. *Desalination* **308**, 34–40 (2013). doi:10.1016/j.desal.2012.07.007
6. Y. X. Shen, W. Si, M. Erbakan, K. Decker, R. De Zorzi, P. O. Saboe, Y. J. Kang, S. Majd, P. J. Butler, T. Walz, A. Aksimentiev, J. L. Hou, M. Kumar, Highly permeable artificial water channels that can self-assemble into two-dimensional arrays. *Proc. Natl. Acad. Sci. U.S.A.* **112**, 9810–9815 (2015). doi:10.1073/pnas.1508575112 [Medline](#)
7. M. Barboiu, A. Gilles, From natural to bioassisted and biomimetic artificial water channel systems. *Acc. Chem. Res.* **46**, 2814–2823 (2013). doi:10.1021/ar400025e [Medline](#)
8. B. Corry, Designing carbon nanotube membranes for efficient water desalination. *J. Phys. Chem. B* **112**, 1427–1434 (2008). doi:10.1021/jp709845u [Medline](#)
9. G. Hummer, J. C. Rasaiah, J. P. Noworyta, Water conduction through the hydrophobic channel of a carbon nanotube. *Nature* **414**, 188–190 (2001). doi:10.1038/35102535 [Medline](#)
10. S. Joseph, N. R. Aluru, Why are carbon nanotubes fast transporters of water? *Nano Lett.* **8**, 452–458 (2008). doi:10.1021/nl072385q [Medline](#)
11. M. Majumder, N. Chopra, R. Andrews, B. J. Hinds, Erratum: Nanoscale hydrodynamics: Enhanced flow in carbon nanotubes. *Nature* **438**, 44 (2005). doi:10.1038/438930b
12. J. K. Holt, H. G. Park, Y. Wang, M. Stadermann, A. B. Artyukhin, C. P. Grigoropoulos, A. Noy, O. Bakajin, Fast mass transport through sub-2-nanometer carbon nanotubes. *Science* **312**, 1034–1037 (2006). doi:10.1126/science.1126298 [Medline](#)
13. E. Secchi, S. Marbach, A. Niguès, D. Stein, A. Siria, L. Bocquet, Massive radius-dependent flow slippage in carbon nanotubes. *Nature* **537**, 210–213 (2016). doi:10.1038/nature19315 [Medline](#)
14. F. Fornasiero, H. G. Park, J. K. Holt, M. Stadermann, C. P. Grigoropoulos, A. Noy, O. Bakajin, Ion exclusion by sub-2-nm carbon nanotube pores. *Proc. Natl. Acad. Sci. U.S.A.* **105**, 17250–17255 (2008). doi:10.1073/pnas.0710437105 [Medline](#)
15. J. Geng, K. Kim, J. Zhang, A. Escalada, R. Tunuguntla, L. R. Comolli, F. I. Allen, A. V. Shnyrova, K. R. Cho, D. Munoz, Y. M. Wang, C. P. Grigoropoulos, C. M. Ajo-Franklin,

- V. A. Frolov, A. Noy, Stochastic transport through carbon nanotubes in lipid bilayers and live cell membranes. *Nature* **514**, 612–615 (2014). doi:10.1038/nature13817 [Medline](#)
16. A. Milon, T. Lazrak, A.-M. Albrecht, G. Wolff, G. Weill, G. Ourisson, Y. Nakatani, Osmotic swelling of unilamellar vesicles by the stopped-flow light scattering method. Influence of vesicle size, solute, temperature, cholesterol and three α,ω -dihydroxycarotenoids. *Biochim. Biophys. Acta* **859**, 1–9 (1986). doi:10.1016/0005-2736(86)90311-1
17. Materials and methods are available as supplementary materials..
18. K. Murata, K. Mitsuoka, T. Hirai, T. Walz, P. Agre, J. B. Heymann, A. Engel, Y. Fujiyoshi, Structural determinants of water permeation through aquaporin-1. *Nature* **407**, 599–605 (2000). doi:10.1038/35036519 [Medline](#)
19. A. Horner, F. Zocher, J. Preiner, N. Ollinger, C. Siligan, S. A. Akimov, P. Pohl, The mobility of single-file water molecules is governed by the number of H-bonds they may form with channel-lining residues. *Sci. Adv.* **1**, e1400083 (2015). doi:10.1126/sciadv.1400083 [Medline](#)
20. B. Corry, Water and ion transport through functionalised carbon nanotubes: Implications for desalination technology. *Energy Environ. Sci.* **4**, 751–759 (2011). doi:10.1039/c0ee00481b
21. E. Schwegler, J. C. Grossman, F. Gygi, G. Galli, Towards an assessment of the accuracy of density functional theory for first principles simulations of water. II. *J. Chem. Phys.* **121**, 5400–5409 (2004). doi:10.1063/1.1782074 [Medline](#)
22. B. L. de Groot, H. Grubmüller, Water permeation across biological membranes: Mechanism and dynamics of aquaporin-1 and GlpF. *Science* **294**, 2353–2357 (2001). doi:10.1126/science.1062459 [Medline](#)
23. H. Uedaira, H. Uedaira, Role of hydration of polyhydroxy compounds in biological systems. *Cell. Mol. Biol.* **47**, 823–829 (2001). [Medline](#)
24. R. Mills, Self-diffusion in normal and heavy water in the range 1–45 deg. *J. Phys. Chem.* **77**, 685–688 (1973). doi:10.1021/j100624a025
25. P. H. Nelson, A permeation theory for single-file ion channels: Corresponding occupancy states produce Michaelis–Menten behavior. *J. Chem. Phys.* **117**, 11396–11403 (2002). doi:10.1063/1.1522709
26. E. Secchi, A. Niguès, L. Jubin, A. Siria, L. Bocquet, Scaling behavior for ionic transport and its fluctuations in individual carbon nanotubes. *Phys. Rev. Lett.* **116**, 154501 (2016). doi:10.1103/PhysRevLett.116.154501 [Medline](#)
27. H. Amiri, K. L. Shepard, C. Nuckolls, R. Hernández Sánchez, Single-walled carbon nanotubes: Mimics of biological ion channels. *Nano Lett.* **17**, 1204–1211 (2017). doi:10.1021/acs.nanolett.6b04967 [Medline](#)
28. P. M. Biesheuvel, M. Z. Bazant, Analysis of ionic conductance of carbon nanotubes. *Phys. Rev. E* **94**, 050601 (2016). doi:10.1103/PhysRevE.94.050601 [Medline](#)
29. J. Wu, X. Zhan, B. J. Hinds, Ionic rectification by electrostatically actuated tethers on single walled carbon nanotube membranes. *Chem. Commun. (Camb.)* **48**, 7979–7981 (2012). doi:10.1039/c2cc33355d [Medline](#)

30. P. Ramirez, V. Gomez, J. Cervera, S. Nasir, M. Ali, W. Ensinger, Z. Siwy, S. Mafe, Voltage-controlled current loops with nanofluidic diodes electrically coupled to solid state capacitors. *RSC Advances* **6**, 54742–54746 (2016). doi:10.1039/C6RA08277G
31. M. L. Zeidel, S. V. Ambudkar, B. L. Smith, P. Agre, Reconstitution of functional water channels in liposomes containing purified red cell CHIP28 protein. *Biochemistry* **31**, 7436–7440 (1992). doi:10.1021/bi00148a002 [Medline](#)
32. D. J. Tobias, J. C. Hemminger, Getting specific about specific ion effects. *Science* **319**, 1197–1198 (2008). doi:10.1126/science.1152799 [Medline](#)
33. F. Zhu, E. Tajkhorshid, K. Schulten, Collective diffusion model for water permeation through microscopic channels. *Phys. Rev. Lett.* **93**, 224501 (2004). doi:10.1103/PhysRevLett.93.224501 [Medline](#)
34. G. Soveral, C. Prista, T. F. Moura, M. C. Loureiro-Dias, Yeast water channels: An overview of orthodox aquaporins. *Biol. Cell* **103**, 35–54 (2011). doi:10.1042/BC20100102 [Medline](#)
35. R. H. Tunuguntla, A. Escalada, V. A. Frolov, A. Noy, Synthesis, lipid membrane incorporation, and ion permeability testing of carbon nanotube porins. *Nat. Protoc.* **11**, 2029–2047 (2016). doi:10.1038/nprot.2016.119 [Medline](#)
36. R. H. Tunuguntla, F. I. Allen, K. Kim, A. Belliveau, A. Noy, Ultrafast proton transport in sub-1-nm diameter carbon nanotube porins. *Nat. Nanotechnol.* **11**, 639–644 (2016). doi:10.1038/nnano.2016.43 [Medline](#)
37. R. H. Tunuguntla, X. Chen, A. Belliveau, F. I. Allen, A. Noy, High-yield synthesis and optical properties of carbon nanotube porins. *J. Phys. Chem. C* **121**, 3117–3125 (2017). doi.org/10.1021/acs.jpcc.6b11658
38. P. Latimer, B. E. Pyle, Light scattering at various angles. Theoretical predictions of the effects of particle volume changes. *Biophys. J.* **12**, 764–773 (1972). doi:10.1016/S0006-3495(72)86120-4 [Medline](#)
39. J. de Gier, Osmotic behaviour and permeability properties of liposomes. *Chem. Phys. Lipids* **64**, 187–196 (1993). doi:10.1016/0009-3084(93)90065-B [Medline](#)
40. J. M. Carbrey, D. A. Gorelick-Feldman, D. Kozono, J. Praetorius, S. Nielsen, P. Agre, Aquaglyceroporin AQP9: Solute permeation and metabolic control of expression in liver. *Proc. Natl. Acad. Sci. U.S.A.* **100**, 2945–2950 (2003). doi:10.1073/pnas.0437994100 [Medline](#)
41. K. Liu, H. Nagase, C. G. Huang, G. Calamita, P. Agre, Purification and functional characterization of aquaporin-8. *Biol. Cell* **98**, 153–161 (2006). doi:10.1042/BC20050026 [Medline](#)
42. D. Kozono, X. Ding, I. Iwasaki, X. Meng, Y. Kamagata, P. Agre, Y. Kitagawa, Functional expression and characterization of an archaeal aquaporin: AqpM from *Methanothermobacter marburgensis*. *J. Biol. Chem.* **278**, 10649–10656 (2003). doi:10.1074/jbc.M212418200 [Medline](#)
43. B. Yang, A. N. van Hoek, A. S. Verkman, Very high single channel water permeability of aquaporin-4 in baculovirus-infected insect cells and liposomes reconstituted with purified aquaporin-4. *Biochemistry* **36**, 7625–7632 (1997). doi:10.1021/bi970231r [Medline](#)

44. M. J. Borgnia, D. Kozono, G. Calamita, P. C. Maloney, P. Agre, Functional reconstitution and characterization of AqpZ, the *E. coli* water channel protein. *J. Mol. Biol.* **291**, 1169–1179 (1999). doi:10.1006/jmbi.1999.3032 [Medline](#)
45. J. L. Rigaud, M. T. Paternostre, A. Bluzat, Mechanisms of membrane protein insertion into liposomes during reconstitution procedures involving the use of detergents. 2. Incorporation of the light-driven proton pump bacteriorhodopsin. *Biochemistry* **27**, 2677–2688 (1988). doi:10.1021/bi00408a007 [Medline](#)
46. P. W. Holloway, A simple procedure for removal of Triton X-100 from protein samples. *Anal. Biochem.* **53**, 304–308 (1973). doi:10.1016/0003-2697(73)90436-3 [Medline](#)
47. N. Kučerka, S. Tristram-Nagle, J. F. Nagle, Structure of fully hydrated fluid phase lipid bilayers with monounsaturated chains. *J. Membr. Biol.* **208**, 193–202 (2006). doi:10.1007/s00232-005-7006-8 [Medline](#)
48. V. Tabard-Cossa, D. Trivedi, M. Wiggin, N. N. Jetha, A. Marziali, Noise analysis and reduction in solid-state nanopores. *Nanotechnology* **18**, 305505 (2007). doi:10.1088/0957-4484/18/30/305505
49. K. Kumar, L. Isa, A. Egner, R. Schmidt, M. Textor, E. Reimhult, Formation of nanopore-spanning lipid bilayers through liposome fusion. *Langmuir* **27**, 10920–10928 (2011). doi:10.1021/la2019132 [Medline](#)
50. B. M. Venkatesan, J. Polans, J. Comer, S. Sridhar, D. Wendell, A. Aksimentiev, R. Bashir, Lipid bilayer coated Al₂O₃ nanopore sensors: Towards a hybrid biological solid-state nanopore. *Biomed. Microdevices* **13**, 671–682 (2011). doi:10.1007/s10544-011-9537-3 [Medline](#)
51. A. Alcaraz, E. M. Nestorovich, M. Aguilera-Arzo, V. M. Aguilera, S. M. Bezrukov, Salting out the ionic selectivity of a wide channel: The asymmetry of OmpF. *Biophys. J.* **87**, 943–957 (2004). doi:10.1529/biophysj.104/043414 [Medline](#)
52. W. M. Haynes, *CRC Handbook of Chemistry and Physics* (CRC Press, 2014).
53. D. K. Kim, C. H. Duan, Y. F. Chen, A. Majumdar, Power generation from concentration gradient by reverse electrodialysis in ion-selective nanochannels. *Microfluid. Nanofluidics* **9**, 1215–1224 (2010). doi:10.1007/s10404-010-0641-0
54. J. P. Perdew, K. Burke, M. Ernzerhof, Generalized gradient approximation made simple. *Phys. Rev. Lett.* **77**, 3865–3868 (1996). doi:10.1103/PhysRevLett.77.3865 [Medline](#)
55. T. A. Pham, S. M. G. Mortuza, B. C. Wood, E. Y. Lau, T. Ogitsu, S. F. Buchsbaum, Z. S. Siwy, F. Fornasiero, E. Schwegler, Salt solutions in carbon nanotubes: The role of cation- π interactions. *J. Phys. Chem. C* **120**, 7332–7338 (2016). doi:10.1021/acs.jpcc.5b12245
56. H. J. Choi, J.-M. Song, B. J. Bondy, R. W. Compans, S.-M. Kang, M. R. Prausnitz, Effect of osmotic pressure on the stability of whole inactivated influenza vaccine for coating on microneedles. *PLoS One* **10**, e0134431 (2015). doi:10.1371/journal.pone.0134431 [Medline](#)

57. N. P. Illsley, A. S. Verkman, Serial permeability barriers to water transport in human placental vesicles. *J. Membr. Biol.* **94**, 267–278 (1986). [doi:10.1007/BF01869722](https://doi.org/10.1007/BF01869722) [Medline](#)
58. N. Kučerka, S. Tristram-Nagle, J. F. Nagle, Closer look at structure of fully hydrated fluid phase DPPC bilayers. *Biophys. J.* **90**, L83–L85 (2006). [doi:10.1529/biophysj.106.086017](https://doi.org/10.1529/biophysj.106.086017) [Medline](#)
59. J. C. Mathai, S. Tristram-Nagle, J. F. Nagle, M. L. Zeidel, Structural determinants of water permeability through the lipid membrane. *J. Gen. Physiol.* **131**, 69–76 (2008). [doi:10.1085/jgp.200709848](https://doi.org/10.1085/jgp.200709848) [Medline](#)
60. A. Finkelstein, *Water Movement through Lipid Bilayers, Pores, and Plasma-Membranes: Theory and Reality* (Wiley, New York, 1987).
61. E. M. Renkin, Filtration, diffusion, and molecular sieving through porous cellulose membranes. *J. Gen. Physiol.* **38**, 225–243 (1954). [Medline](#)
62. C. V. Paganelli, A. K. Solomon, The rate of exchange of tritiated water across the human red cell membrane. *J. Gen. Physiol.* **41**, 259–277 (1957). [doi:10.1085/jgp.41.2.259](https://doi.org/10.1085/jgp.41.2.259) [Medline](#)
63. S. Paula, M. Akeson, D. Deamer, Water transport by the bacterial channel α -hemolysin. *Biochim. Biophys. Acta* **1418**, 117–126 (1999). [doi:10.1016/S0005-2736\(99\)00031-0](https://doi.org/10.1016/S0005-2736(99)00031-0) [Medline](#)
64. B. Radha, A. Esfandiari, F. C. Wang, A. P. Rooney, K. Gopinadhan, A. Keerthi, A. Mishchenko, A. Janardanan, P. Blake, L. Fumagalli, M. Lozada-Hidalgo, S. Garaj, S. J. Haigh, I. V. Grigorieva, H. A. Wu, A. K. Geim, Molecular transport through capillaries made with atomic-scale precision. *Nature* **538**, 222–225 (2016). [doi:10.1038/nature19363](https://doi.org/10.1038/nature19363) [Medline](#)
65. A. Berezhkovskii, G. Hummer, Single-file transport of water molecules through a carbon nanotube. *Phys. Rev. Lett.* **89**, 064503 (2002). [doi:10.1103/PhysRevLett.89.064503](https://doi.org/10.1103/PhysRevLett.89.064503) [Medline](#)
66. T. Gutschmann, T. Heimburg, U. Keyser, K. R. Mahendran, M. Winterhalter, Protein reconstitution into freestanding planar lipid membranes for electrophysiological characterization. *Nat. Protoc.* **10**, 188–198 (2015). [doi:10.1038/nprot.2015.003](https://doi.org/10.1038/nprot.2015.003) [Medline](#)
67. L.-Q. Gu, M. Dalla Serra, J. B. Vincent, G. Vigh, S. Cheley, O. Braha, H. Bayley, Reversal of charge selectivity in transmembrane protein pores by using noncovalent molecular adapters. *Proc. Natl. Acad. Sci. U.S.A.* **97**, 3959–3964 (2000). [doi:10.1073/pnas.97.8.3959](https://doi.org/10.1073/pnas.97.8.3959) [Medline](#)
68. V. B. Myers, D. A. Haydon, Ion transfer across lipid membranes in the presence of gramicidin A. II. The ion selectivity. *Biochim. Biophys. Acta* **274**, 313–322 (1972). [doi:10.1016/0005-2736\(72\)90179-4](https://doi.org/10.1016/0005-2736(72)90179-4) [Medline](#)